Mag-ODO: Motion speed estimation for indoor robots based on dual magnetometers

Tisheng Zhang [a], Linfu Wei [a], Jian Kuang [a,*], Hailiang Tang [a], Xiaoji Niu [a,b]

[a] *GNSS Research Center, Wuhan University, Wuhan 430072, China*
[b] *Artificial Intelligence Institute, Wuhan University, Wuhan 430072, China*

ARTICLE INFO	ABSTRACT
Keywords: Magnetic field odometer Speed estimation Indoor positioning Robot positioning Dead reckoning Waveform matching	In indoor environments, accurate speed estimation is crucial for providing continuous and reliable position of mobile robots. However, conventional odometry methods may suffer from performance degradation, particularly in scenarios involving wheel odometry slipping or visual odometry blurring. In this study, we propose Mag-ODO, a novel motion speed estimation method based on dual magnetometers aimed at enhancing the robustness of indoor robot positioning systems. The dual magnetometers are mounted at the front and back of the robot, and the speed is estimated by matching the magnetic-filed waveforms sampled from the magnetometers. We employ the dynamic time warping (DTW) algorithm to implement waveform matching and use both the magnetic field strengths and the changing trend of the magnetic field strengths as the matching cost function, effectively reducing the matching error. Mag-ODO has two key advantages: immunity to magnetometer bias and transient disappearance of magnetic field gradients within a matching time window does not affect speed estimation accuracy. Test results show that Mag-ODO performs similarly to Wheel-ODO in magnetic-rich environments (RMSE < 0.06 m/s) and comparable dead reckoning (DR) performance with inertial navigation systems (INS) in both straight and curved environments.

1. Introduction

Accurate and robust position and heading estimation for mobile robots has become more and more essential for autonomous mobile robots [1]. The Global Navigation Satellite System (GNSS) can provide reliable navigation and positioning capabilities, but it is unusable for indoor applications [2]. Dead reckoning (DR) is a commonly used self-contained positioning method in GNSS-denied environments. DR systems can estimate the position and attitude by integrating linear and angular velocity measurements. Typically, DR systems consist of an inertial measurement unit (IMU) and an odometry [3]. IMU can provide angular velocity measurements, and odometry can provide linear velocity measurements. Therefore, accurate and robust odometry is essential for DR systems. Consequently, research on self-contained odometry systems has recently attracted much attention [4].

According to our investigation, there are four main types of odometry [4], including the wheel odometry, the inertial odometry, the LiDAR odometry, and the visual odometry. The strengths and weaknesses of the above odometry are shown in Table 1 [5–11]. Despite the advantages, these odometry methods can suffer from performance degradation in certain scenarios, as shown in Table 1, leading to reduced robustness in the navigation system. Other low-cost sensors can be employed to enhance the robustness of these systems. One promising candidate is the magnetometer.

The magnetometer-based velocity estimation method was first proposed by David Vissière et al. in 2007 [12,13]. This method is based on Maxwell equations and aims to estimate inertial velocity by utilizing indoor magnetic field disturbances, requiring no prior mapping or other information. Hence, it has been further investigated by other researchers [14–17]. Charles-Ivan Chesneau demonstrated strap-down inertial navigation technology assisted by magnetic field features, indoor DR technology based on Micro-Electro-Mechanical System (MEMS) Magnetometer and MEMS IMU, and calibration technology of magnetometer arrays [18]. Makia Zmitri *et al.* proposed an extended Kalman filter (EKF) based magnetic field gradient estimation method to reduce noise affecting magnetic field gradients [19]. More recently, Isaac Skog *et al.* proposed using optical flow methods in image processing to extract velocity information from magnetometer array data [20].

Although the methods mentioned above can provide velocity information without requiring prior magnetic field information or a map,

---

* Corresponding author.
   E-mail address: kuang@whu.edu.cn (J. Kuang).

Table 1

Comparison of Typical odometry.

Odometry Type	Advantage	Disadvantage
Wheel odometry [9]	Easy to mount on wheeled robots; Low cost.	The performance would degrade due to slippage on tough surface.
Inertial odometry	Fully self-contained[810]; Low cost.	Drift issue due to the influence of error factors such as gyroscope bias and accelerometer bias. [5]
LiDAR odometry	Insensitive to light changes and low-texture environments; Perform well in structured scenes. [11]	High cost; Appear degeneracy arose by the lack of geometrical structures. [6]
Visual odometry	Performs well in the texture-rich environment. [7]	Vulnerable to light changes and lack of visual texture. [11]

they all rely on a magnetometer array to obtain magnetic field measurements, necessitating strict installation and calibration. Nevertheless, even after rigorous installation and calibration, the magnetometer bias may change significantly due to alterations in hardware structure and working conditions, as well as random bias, which limits the applicability of these methods. Additionally, these methods are sensitive to magnetic field gradients, rendering them ineffective in areas where the magnetic field gradient is not apparent.

In this study, we introduce Mag-ODO, a low-cost dual-magnetometer-based speed estimation method. This method employs waveform matching to associate the measurements of the front and back magnetometers passing through the same position at different times and combines the fixed distances of the two magnetometers to obtain the carrier's speed. This method takes advantage of the fact that the vertical projection of the magnetometer bias is a constant value [21] and uses the changing trend of the vertical component of the magnetic field as one of the matching indicators, thereby effectively eliminating the influence of the magnetometer bias on the matching results. In addition, the method uses a time window to match the waveforms, effectively reducing the influence of the temporary disappearance of the magnetic field gradient within the time window on the matching results. The matching fails only when the magnetic field gradient within the window completely disappears. Therefore, the method proposed in this study is more tolerant to magnetic field gradient disappearance.

Fig. 1 illustrates the algorithm structure of DR based on Mag-ODO and the Inertial Navigation System (INS). In this algorithm, INS Mechanization predicts the state of the carrier, while Mag-ODO provides the speed measurement. An EKF is employed for information fusion, and the estimated state errors are used to update the robot pose and compensate

for the IMU outputs.

In this study, we make several noteworthy contributions. Firstly, we propose a novel speed estimation method called Mag-ODO, based on the time difference between the front and back magnetometers passing the same position at different times. Secondly, we conduct field tests to evaluate the Mag-ODO's characteristics fully. The experimental results demonstrate that the Mag-ODO performs almost as well as the wheel odometer. Thirdly, we implement a DR system based on MEMS-IMU and Mag-ODO to evaluate its performance further. A comparison between Mag-ODO/INS and Wheel-ODO/INS is carried out, and the results show that the Mag-ODO/INS has nearly the same performance as the Wheel-ODO/INS in environments with rich magnetic field features.

The rest of the paper is organized as follows. Section 2 provides a detailed description of the proposed Mag-ODO method. Section 3 presents the fusion algorithm used in our system. Section 4 analyzes the testing results obtained from our experiments. Finally, we conclude the proposed methods and present future work in Section 5.

2. Methodology

In general, carriers cannot be considered a single mass point but a rigid body. Therefore, when a carrier moves, different parts of the carrier pass through nearly the same position at different times. This results in a time difference between the front and back parts of the carrier passing through the same position. The time difference is inversely proportional to the speed of the carrier, allowing us to obtain the speed of the carrier by measuring this time difference. However, how to perceive that the two parts of the carrier have passed the same position? We can solve it with two magnetometers mounted on the front and back positions of the carrier. Most indoor environments have many different magnetic features [22]. The magnetic field features at different indoor positions differ due to artificial ferromagnetic materials. Furthermore, the magnetic field strength exhibits a cubic decay with distance from the ferromagnetic material [23], and the spatial resolution of the magnetic field is sufficiently high. These facts allow us to obtain the time difference between the front and back magnetometers passing by the same position by matching the measurements of the two magnetometers.

Fig. 2. illustrates the working principle of Mag-ODO. Two magnetometers are mounted on the front and back of the carrier, respectively, and produce similar magnetic field waveforms as the carrier moves. By matching the waveforms sample by sample, we can obtain the time difference between the two magnetometers passing the same position. Then, we calculate the moving speed using the time difference and the fixed distance between the magnetometers.

It should be noted that the magnetic field at the same position will remain relatively constant over time if there is no external interference
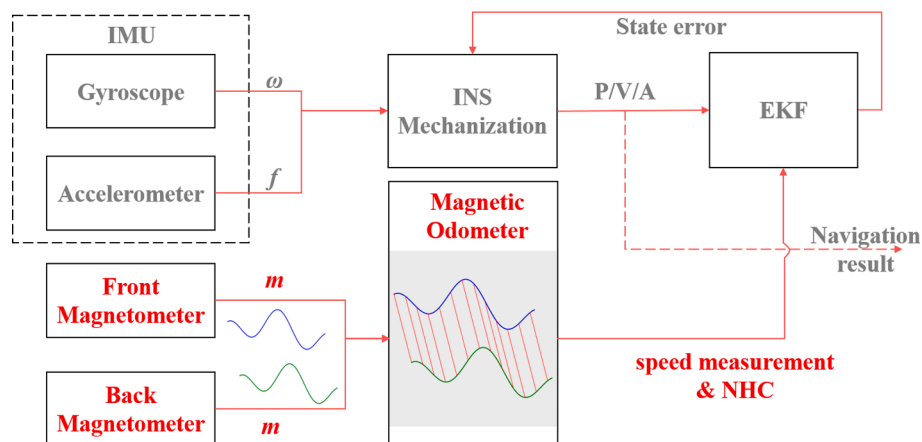
Fig. 1. DR algorithm structure. P/V/A represent position, velocity, and attitude, respectively. NHC represents non-holonomic constraints, ω represents gyroscope measurements, *f* represents accelerometer measurements, and *m* represents magnetometer measurements.
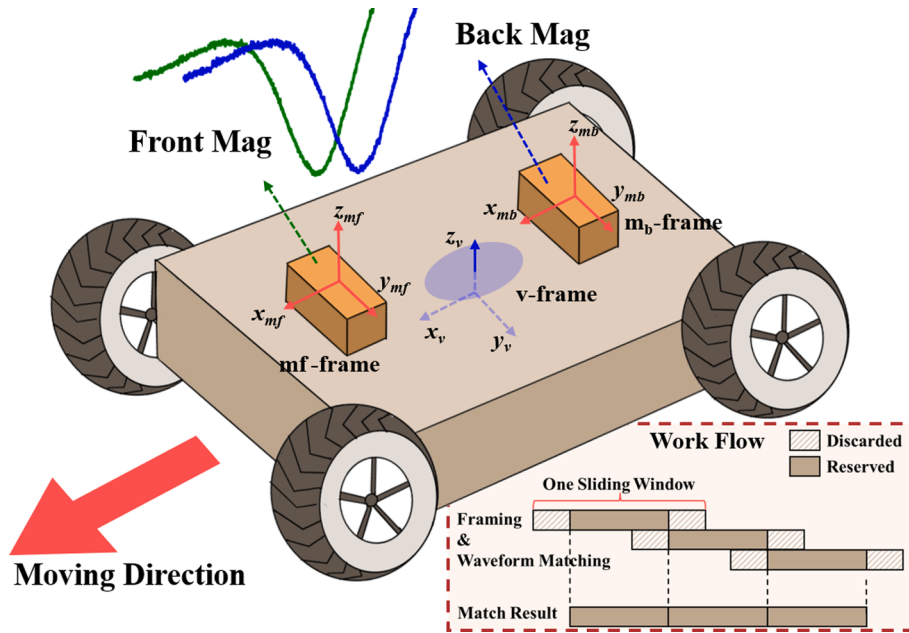
Fig. 2. Installation and work flow of the Mag-ODO.

or the interfering source is stationary. Therefore, in such cases, Mag-ODO is not affected by temporal variations in the magnetic field. Moreover, if a moving ferromagnetic material is nearby, Mag-ODO can still function properly as long as the magnetic field remains constant when the front and back magnetometers pass through that material.

Let f represent the sampling frequency of the magnetometer, L represent the distance between the front and back magnetometers, and N represent the number of samples that differ between the sample of the back magnetometer and its corresponding sample of the front magnetometer obtained by waveform matching. The speed of the carrier can be calculated as follows:

$$v = \frac{Lf}{N} \tag{1}$$

From Equation (1), it can be observed that the speed estimation results are dependent on the distance, L, between the magnetometers. If the carrier maintains a linear and constant speed motion, a larger L would lead to higher accuracy in speed estimation. However, in practical applications, the trajectory of the carrier is uncertain, and as L increases, the uncertainty of the matching results also increases. As the trajectory shape becomes more complex, the spatial structure experienced by the front and back magnetometers is not completely consistent, which will result in speed estimation errors.

2.1. Installation scheme and coordinate systems

Fig. 2 illustrates how the Mag-ODO is installed, while Fig. 3 defines the relevant coordinate systems. The vehicle coordinate system is denoted by the v-frame, where the x-axis points forward, the y-axis
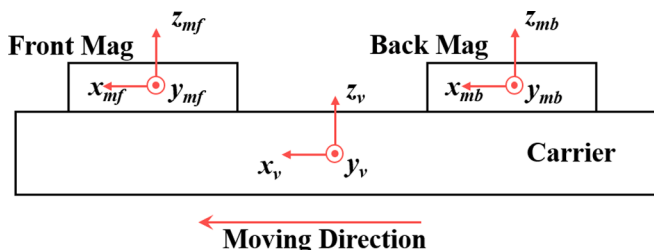
points left, and the z-axis points up, forming a right-handed orthogonal frame (*i.e.*, the forward-left-up system). The origin of the v-frame is typically set at the center of mass of the vehicle. The coordinate systems of the front and back magnetometers are represented by the mf-frame and mb-frame, respectively.

Before installing the magnetometers, it is important to determine which magnetic field axis is more suitable for estimating the speed of motion. In this method, the z-axis is considered more suitable due to its parallelism with the robot's z-axis and the convenience of installation without any restriction on the directions of the × and y axes, which may lead to more complicated issues related to mounting angle. Therefore, z-axis data are chosen for waveform matching.

During the installation of the magnetometers, it can be challenging to ensure that the z-axis of the two magnetometers' coordinate systems is entirely parallel to the z-axis of the v-frame, and the initial bias of the two magnetometers may be different, causing differences in their waveforms. To address this, the waveform matching algorithm used in this study considers both the magnetic field strength and its variation trend to eliminate the influence of incomplete parallelism and initial zero bias. While it is important to make the z-axis of the magnetometer coordinate system and the v-frame as parallel as possible, it is not strictly necessary. Mounting the magnetometers vertically on the carrier plane is sufficient for simplified operation.

Meanwhile, ensuring that the line connecting the origins of the two magnetometer coordinate systems is parallel to the x-axis of the v-frame is challenging, which can affect the final speed calculation. Let L represent the magnetometer distance, L' represent the projection of the magnetometer distance on the x-axis of the *v*-frame. A small misalignment between the origin of the two magnetometers coordinate systems and the x-axis of the v-frame is denoted by $\delta\psi$, then $L' = L \cos(\delta\psi)$. Based on the small angle assumption, L' can be approximated as $L(1-\delta\psi)$. As $v = L'/\Delta t$, the misalignment $\delta\psi$ can be considered as the scale factor of the speed observation, and it can be estimated through multi-sensor information fusion (such as GNSS/INS/ODO loose coupling). In this study, we perform calibration in advance to eliminate the influence of the misalignment.

It should be noted that the magnetometer used in this study has almost no limitation on accuracy, and two MEMS magnetometers would be sufficient. However, during usage, careful attention should be given to the installation position of the magnetometer. It is advisable to place

Fig. 3. Definition of the relevant coordinate systems.

the magnetometer as far away as possible from sources of interference, such as motors and power supplies, to avoid any influence of fluctuating magnetic fields on accuracy. Once installed, the position of the magnetometer should be kept unchanged to ensure consistent and reliable measurements. In addition, the application scenario should also be considered. The magnetic field in the environment should remain stable and should not fluctuate significantly. During operation, the robot should be kept away from moving ferromagnetic objects, which will interfere with the magnetic field and affect the accuracy of the magnetic field odometer.

2.2. Speed calculation principle

The Mag-ODO workflow involves several steps. First, the front and back magnetometer measurements are collected. Next, the measurements undergo preprocessing, which includes low-pass filtering, framing, and normalization. The preprocessed measurements are then matched using waveform matching. Fig. 4 shows the framing and waveform matching process. The matching results of the beginning and ending times The reason will be described later. Additionally, adjacent frames have partial overlap, and the final matching result is obtained by splicing the matching results of all time windows. We use the dynamic time warping (DTW) algorithm for waveform matching, and more details about this algorithm will be provided later.

Ensuring high-precision matching of the magnetic field waveforms is crucial to the success of the Mag-ODO system. Among the algorithms commonly used for waveform matching, such as the correlation coefficient method [24] and DTW [25], DTW is more appropriate for this task since the speed of the carrier varies with time. The idea behind DTW is to find the optimal path for matching two signals by warping their time scales. We use the Dijkstra algorithm, commonly used in path planning [26], to implement the DTW algorithm. By integrating the kinematic constraints of the carrier, such as its speed and acceleration, into the cost matrix and search space, we can achieve a highly accurate match.

Except for the setting of the cost matrix, the rest of the proposed matching algorithm is the same as the typical Dijkstra algorithm. The cost matrix is used to describe the similarity between each point of the waveforms. A lower cost indicates a higher similarity. Typically, the Euclidean distance is used as the cost between two points. However, the measurements from the two magnetometers may not be equal due to magnetometer bias or fixed magnetic interference, and the z-axis of the magnetometer coordinate system may not be parallel. The former can be compensated partially during the initialization of the Mag-ODO but cannot be eliminated. To address these issues, we include the changing trend of the magnetic field strength as part of the cost. In paper [27], the changing trend of the i-th point is defined using a derivative calculation method as follows.

$$div(p_i) = \frac{(p_i - p_{i-1}) + ((p_{i+1} - p_{i-1})/2)}{2} \tag{2}$$

where p_i represents the data of the i-th point, and $div(p_i)$ represents the changing trend of the i-th point.

To summarize, the cost between two samples is defined as follows:

$$cost(p_i, p_j) = dist(p_i, p_j) + dist(div(p_i), div(p_j)) \tag{3}$$

where $cost(p_i, p_j)$ represents the degree of difference between the i-th point and the j-th point. The first term on the right side of the equation represents the Euclidean distance between the i-th point and the j-th point, while the second term represents the Euclidean distance of changing trend of the i-th point and the j-th point.

Fig. 5 illustrates the matching results obtained using three different cost functions. It is worth noting that both (a) and (b) failed to align the two central peaks, meaning that the two troughs in (a) were not matched, while there were several mismatch points between the two troughs in (b). This result highlights that relying on only one of the two items is insufficient to achieve an excellent match, whereas incorporating both items yields satisfactory results.

Upon observing the matching results in Fig. 5 (c), it can be seen that there are several mismatches at the beginning and end of the waveforms. The front magnetometer has no corresponding data with the back magnetometer at the beginning of the sliding window, while the back magnetometer has no corresponding data with the front magnetometer at the end of the sliding window. To address this, we remove the mismatches at both ends while retaining the matching result of the middle region. Fig. 6 illustrates the matching results after removing the mismatches. With the matching completed, each sample of the back magnetometer can now find a corresponding sample in the front magnetometer waveform. The speed of the carrier is then calculated using Equation (1). Fig. 7 shows the speed results with and without the removal of mismatches. The speed curve without removing mismatches has many abnormal spikes, while the speed curve with removing mismatches agrees well with the wheel odometer.

3. Fusion algorithm design

An EKF algorithm is utilized to fuse the Mag-ODO and IMU in order to evaluate the performance of the proposed Mag-ODO in a DR system [28].

3.1. INS Mechanization

The INS Mechanization algorithm is based on the idea that the current position, velocity, and attitude of a moving object can be obtained by integrating acceleration twice and angular rate once, given the initial navigation state. For this study, we use the MEMS-IMU for INS Mechanization. The simplified version of the discrete INS mechanization algorithm equations in the navigation coordinate system (*i.e.*, n-frame) is presented below [22]:
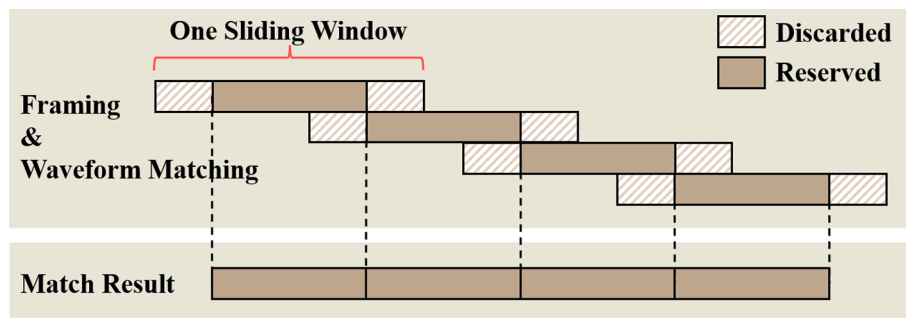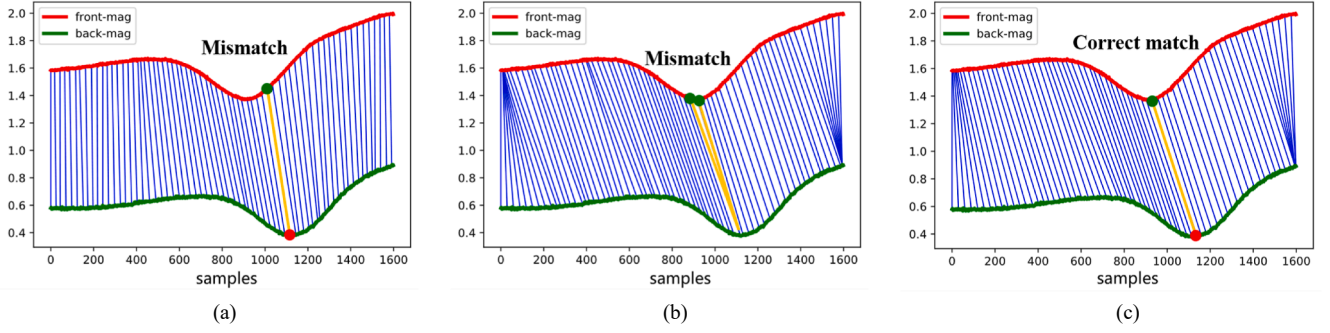

Fig. 4. Framing and waveform matching process.

Fig. 5. Matching results of three different cost functions: (a) Using only the Euclidean distance of the change trend item as the cost, (b) using only the Euclidean distance of magnetic field strength as the cost, and (c) using both the Euclidean distance of magnetic field strength and the Euclidean distance of the change trend item as the cost. Note that in both (a) and (b), the two central peaks failed to align.
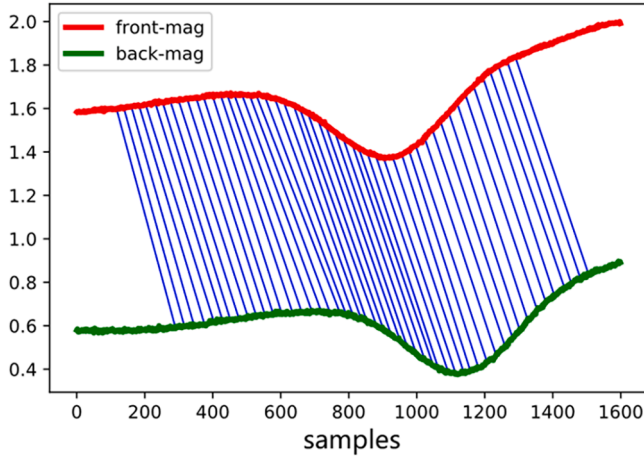
Fig. 6. Matching result of filtering out mismatches.

$$
\begin{bmatrix} \boldsymbol{p}_k^n \\ \boldsymbol{v}_k^n \\ \boldsymbol{C}_{b,k}^n \end{bmatrix} = \begin{bmatrix} \boldsymbol{p}_{k-1}^n + \boldsymbol{v}_k^n \Delta t \\ \boldsymbol{v}_{k-1}^n + \left[\boldsymbol{C}_{b,k}^n \left(\widetilde{\boldsymbol{f}}_k^b - \boldsymbol{b}_a \right) + \boldsymbol{g}^n \right] \Delta t \\ \boldsymbol{C}_{b,k-1}^n + \boldsymbol{C}_{b,k-1}^n \left[\left(\widetilde{\boldsymbol{\omega}}_k^b - \boldsymbol{b}_g \right) \times \right] \Delta t \end{bmatrix} \tag{4}
$$

where $\boldsymbol{p}^n$ and $\boldsymbol{v}^n$ represent the position vector and the velocity vector in the n-frame, respectively, $\boldsymbol{C}_b^n$ represents the transformation matrix from the body coordinate system (*i.e.*, b-frame) to the n-frame, $\boldsymbol{g}^n$ represents the Earth gravity vector in the n-frame, $\widetilde{\boldsymbol{f}}^b$ and $\widetilde{\boldsymbol{\omega}}^b$ represent the acceleration measurement vector and angle rate measurement in the b-frame, respectively. $\boldsymbol{b}_a$ and $\boldsymbol{b}_g$ represent the bias of the accelerometer and gyroscope, respectively. $\Delta t = t_k - t_{k-1}$ represent the time interval between the k-th and (k-1)-th epoch.

3.2. System model

An EKF is used to fuse speed measured by the odometer and INS information. The state vector is usually defined as:

$$
\delta \boldsymbol{x} = \begin{bmatrix} (\delta \boldsymbol{p}^n)^T & (\delta \boldsymbol{v}^n)^T & \boldsymbol{\phi}^T & (\delta \boldsymbol{b}_g)^T & (\delta \boldsymbol{b}_a)^T \end{bmatrix}^T \tag{5}
$$

where δ represents the error of variables, $\delta \boldsymbol{p}^n$, $\delta \boldsymbol{v}^n$ and $\boldsymbol{\phi}$ represent the error vectors of position, velocity, and attitude in the n-frame, respectively. Meanwhile, $\delta \boldsymbol{b}_g$ and $\delta \boldsymbol{b}_a$ represent the error vectors for gyroscope and accelerometer biases, respectively. The discrete linearization of the system error model can be expressed as follows:
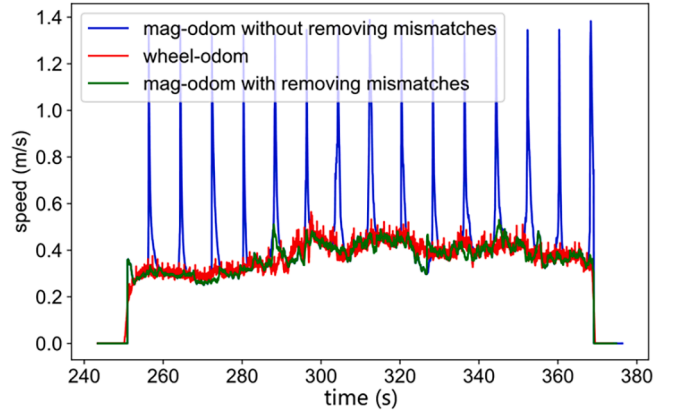
Fig. 7. Speed estimate result with and without removing mismatches.

$$
\begin{cases} \delta \boldsymbol{x}_{k|k-1} = \boldsymbol{\Phi}_{k-1} \delta \boldsymbol{x}_{k-1|k-1} + \boldsymbol{n}_{w,k} \\ \delta \boldsymbol{z}_k = \boldsymbol{H}_k \delta \boldsymbol{x}_{k|k-1} + \boldsymbol{n}_{v,k} \end{cases} \tag{6}
$$

where the subscripts k-1 and k represent the epoch, $\delta \boldsymbol{x}_{k-1|k-1}$ and $\delta \boldsymbol{x}_{k|k-1}$ represent the previous and predicted error state vectors, respectively. $\delta \boldsymbol{z}_k$ represent the measurement misclosure vector, $\boldsymbol{H}_k$ is the observation matrix, $\boldsymbol{n}_{w,k}$, $\boldsymbol{n}_{v,k}$ are the process noise and measurement noise, respectively, and $\boldsymbol{\Phi}_k$ is the 15×15 state transition matrix [28]:

$$
\boldsymbol{\Phi}_k = \begin{bmatrix} \boldsymbol{I}_{3\times3} & \boldsymbol{I}_{3\times3}\Delta t & \boldsymbol{0}_{3\times3} & \boldsymbol{0}_{3\times3} & \boldsymbol{0}_{3\times3} \\ \boldsymbol{0}_{3\times3} & \boldsymbol{I}_{3\times3} & \left(\boldsymbol{f}_k^n \times \right)\Delta t & \boldsymbol{0}_{3\times3} & \boldsymbol{C}_{b,k}^n \Delta t \\ \boldsymbol{0}_{3\times3} & \boldsymbol{0}_{3\times3} & \boldsymbol{I}_{3\times3} & -\boldsymbol{C}_{b,k}^n \Delta t & \boldsymbol{0}_{3\times3} \\ \boldsymbol{0}_{3\times3} & \boldsymbol{0}_{3\times3} & \boldsymbol{0}_{3\times3} & \boldsymbol{I}_{3\times3} & \boldsymbol{0}_{3\times3} \\ \boldsymbol{0}_{3\times3} & \boldsymbol{0}_{3\times3} & \boldsymbol{0}_{3\times3} & \boldsymbol{0}_{3\times3} & \boldsymbol{I}_{3\times3} \end{bmatrix} \tag{7}
$$

3.3. Observation model

The velocity measurement in the v-frame can be expressed as follows:

$$
\widetilde{\boldsymbol{v}}_{odo}^v = \boldsymbol{v}_{odo}^v + \boldsymbol{e}_v \tag{8}
$$

The velocity measurement in the v-frame obtained by the INS Mechanization can be expressed as follows:

$$
\widehat{\boldsymbol{v}}_{odo}^v = \boldsymbol{v}_{odo}^v + \boldsymbol{C}_n^v \left[\boldsymbol{C}_b^n \delta \boldsymbol{v}^n - \boldsymbol{C}_n^b (\boldsymbol{v}^n \times) \boldsymbol{\phi} - \left(\boldsymbol{l}_{odo}^b \times \right) \delta \boldsymbol{\omega}_{ib}^b \right] \tag{9}
$$

where $\boldsymbol{C}_b^v$ represent the IMU mounting angle rotation matrix, $\boldsymbol{l}_{odo}^b$ is the lever arm vector between the b-frame and v-frame. In the DR system based on the Mag-ODO, the origin of the v-frame is the midpoint of the

line connecting the two magnetometers. The measurement vector can be expressed as follows [28]:

$$
\begin{aligned}
\delta z_{odo}^v &= \widehat{v}_{odo}^v - \widetilde{v}_{odo}^v \\
&= C_b^v C_n^b \delta v^n - C_b^v C_n^b (v^n \times) \phi - C_b^v (l_{odo}^b \times) \delta \omega_{ib}^b
\end{aligned}
\tag{10}
$$

The 3×15 measurement matrix can be expressed as follows:

$$
H_k = \begin{bmatrix} 0_{3\times3} & H_{12} & H_{13} & H_{14} & 0_{3\times3} \end{bmatrix}
\tag{11}
$$

where the sub-matrix in H_k is defined as:

$$
\begin{cases}
H_{12} &= C_b^v C_n^{b,k} \\
H_{13} &= -C_b^v C_n^{b,k} \left(v_k^n \times \right) \\
H_{14} &= -C_b^v \left(l_{odo}^b \times \right)
\end{cases}
\tag{12}
$$

4. Experimental result

This section presents experimental results to demonstrate the characteristics of Mag-ODO and its performance in the DR system. The experimental conditions are described first, then the speed measurements obtained from the Mag-ODO and the Wheel-ODO are compared to analyze the Mag-ODO's characteristics. Finally, the DR performances of the Mag-ODO/INS and the Wheel-ODO/INS are compared to demonstrate the practicality of the Mag-ODO in a multi-source positioning system.

4.1. Experimental description

Fig. 8 shows the experimental platform, which includes two self-developed data acquisition modules mounted on the front and back positions of the robot, respectively. Each module includes an inertial sensor chip (ICM20602) and a magnetometer (LIS3MDL), enabling synchronous acquisition of inertial data and magnetic field strength data. The performance parameters of the inertial sensor chip can be found in [29]. The wheel odometer data was also recorded in the Mag-ODO characteristics test, with a resolution of 500 pulses per revolution and a wheel diameter of 7.5 cm. In addition, as depicted in Fig. 8, a 2D LiDAR (RPLIDAR S1) was equipped to provide pose ground truth. The detection range of the LiDAR reaches 40 m, and the sampling frequency is 10 Hz. Based on this LiDAR, the SLAM system can provide decimeter-level positioning results as pose ground truth [30]. To ensure the accuracy of the reference ground truth, we placed several geometric objects strategically within the environment to provide abundant geometric information to the SLAM system, thereby significantly reducing the influence of degenerate scenarios. The primary sensors

Table 2
The main sensors in platform.

Type	Key Parameters	Purpose
ICM20602	Gyro Bias is 200 deg/h, ARW is 0.24 deg/$\sqrt{h}$, Acc. Bias is 0.01 m/s^2, VRW is 3 $m/s/\sqrt{h}$	get raw inertial data for state judgment, time synchronization and DR
LIS3MDL	The output frequency is 200 Hz, the range is set to $-8 \sim 8$ Gauss	get raw magnetometer data for waveforms matching
Wheel odometer	The resolution is 500 pulses per revolution, and the wheel diameter is 7.5 cm	get wheel odometer data for comparing with Mag-ODO
RPLIDAR S1	The detection range of LiDAR reaches 40 m, and the sampling frequency is 10 Hz	provide pose ground truth

used in the experiments are shown in Table 2.

Since the two data acquisition modules operate independently, they cannot collect data synchronously, affecting speed measurement accuracy. We used post-processing to achieve precise time synchronization between the front and back magnetometers to address this issue. In each module, the magnetometer data and the IMU data were synchronized. During post-processing, we indirectly synchronized the magnetometer data by aligning the angular velocity waveforms of the front and back IMUs. It is worth noting that if the two magnetometers are sampled under the same clock, their data can be collected synchronously without post-processing.

In addition, the speed estimation method employed in this study relies on the time difference between the front and back magnetometers passing through the same position. It is only applicable for speed estimation in the dynamic state. Therefore, the experimental evaluation focuses solely on the speed estimation accuracy in the dynamic state, with the motion state obtained through the IMU.

4.2. Mag-ODO characteristics Test

When examining the characteristics of Mag-ODO, we selected a long straight corridor as the test scene to assess the Mag-ODO's performance. The test track, measuring about 43 m, is depicted in Fig. 9. To investigate the impact of the distance between the two magnetometers, we collected magnetometer data at different L values along the same trajectory using four data acquisition modules simultaneously. Fig. 10 illustrates the installation of the four data acquisition modules. By pairing the modules, we obtained the speed measurements of the Mag-ODO at L values of 0.1, 0.2, …, and 0.5 m along the same trajectory.

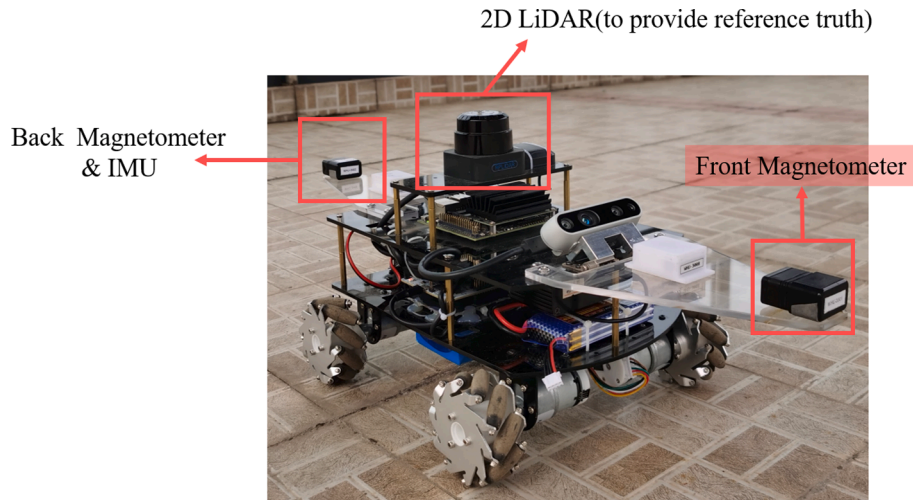The test procedure is as follows. The robot was controlled to move

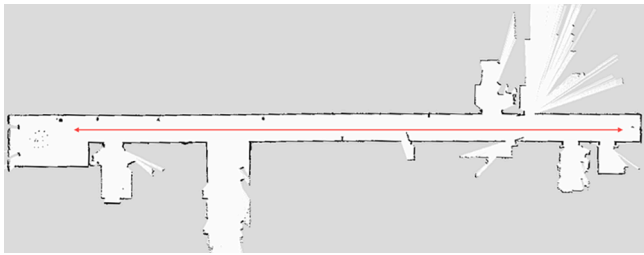**Fig. 8.** Experimental setup used in the study.

Fig. 9. Experimental environment and test trajectory for the Mag-ODO characteristics test.
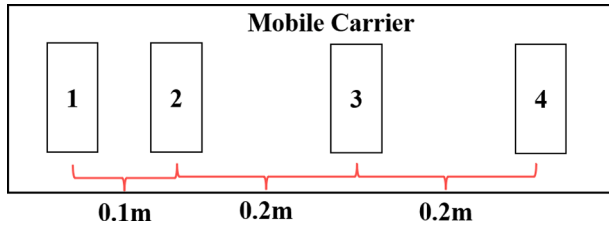

Fig. 10. Installation positions of the four data acquisition modules (*i.e.* magnetometers and IMU) indicated by numbers 1–4.

back and forth three times by a straight trajectory in the corridor, thus reducing the impact of turning. Data from the two magnetic data acquisition modules and the wheel odometer were recorded during this motion. The magnetometer data was processed to obtain the speed of the Mag-ODO. To evaluate the accuracy of the Mag-ODO speed estimation, we calculate the Root Mean Square Error (RMSE) between the Mag-ODO and Wheel-ODO for each test.

1) Influence of the distance between two magnetometers.

The relationship between the RMSE (*i.e.*, the error of the Mag-ODO) and the distance between the magnetometers is shown in Fig. 11. When L is less than 0.4 m, an increase in L leads to an improvement in the performance of the Mag-ODO, approaching that of the wheel odometer. However, when L exceeds 0.4 m, increasing the distance no longer leads to better performance and may even result in slight degradation.

The principle of the Mag-ODO can explain this phenomenon. Assuming a constant speed, an increase in the distance L between the front and back magnetometers leads to an increase in the number of samples N and, thus, an increase in the resolution of speed, indirectly leading to higher accuracy. However, since the robot's trajectory may
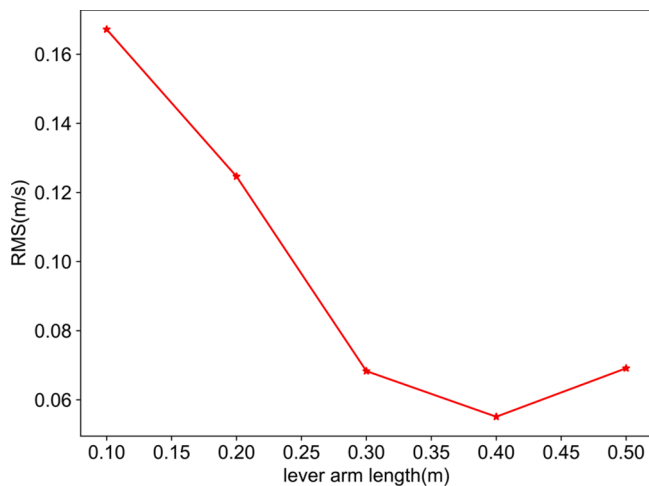
not be perfectly straight, the matching accuracy of the magnetometer data will decrease if L is too large. Therefore, it is necessary to set an appropriate distance (*i.e.*, 0.4 m) between the two magnetometers when using the Mag-ODO.

2) Influence of travel distance within a fixed time window.

The accuracy of the Mag-ODO's speed estimation is highly dependent on the distance traveled by the carrier within a fixed time window. However, determining the travel distance is often not feasible in practical applications. To investigate the impact of this factor, we utilize the wheel odometer to provide the carrier travel distance. We analyze the data from the previous section with $L = 0.4$ m and set the time window length to the time required to travel a fixed distance (given by the wheel odometer). We vary the fixed distance from 0.3 m to 4.2 m in increments of 0.3 m and record the corresponding RMSE values. The resulting curve of RMSE versus the moving distance within a fixed time window is shown in Fig. 12.

As shown in Fig. 12, the accuracy of the Mag-ODO improves and gets closer to the wheel odometer as the travel distance in a fixed time window increases. It is because the matching algorithm requires sequences with enough features to match. With a longer travel distance in a fixed time window, more features can be used for matching, resulting in better-matching results. However, this comes at the cost of increased computation time. Therefore, it is recommended to set an appropriate time window length to balance accuracy and efficiency. It can be observed that the RMSE no longer changes significantly when the travel distance reaches around 2 m, and the moving speed in this study is approximately 0.6 m/s. Therefore, a time window length of 3 s is recommended for this study.

From the above analysis, the following conclusions can be drawn: the faster the speed of the carrier, the longer the distance traveled by the carrier within the same matching window, and the richer the magnetic field features. Therefore, the accuracy of Mag-ODO will be higher.

3) Influence of the complexity of magnetic field features.

To investigate the influence of the complexity of magnetic field features, we conducted tests in three different scenarios: indoor corridor, flat rooftop, and outdoor. The indoor corridor had the richest magnetic field features, followed by the flat rooftop, and the outdoor environment had the sparest features. The speed curves of the Mag-ODO and the wheel odometer in these three scenarios are shown in Fig. 13. The Mag-ODO performed best in the indoor corridor and worst in the outdoor environment. It is because the accuracy of the Mag-ODO is highly dependent on the complexity of the magnetic field features. In environments with rich magnetic field features, the Mag-ODO performs better. Therefore, we recommend using the Mag-ODO in environments
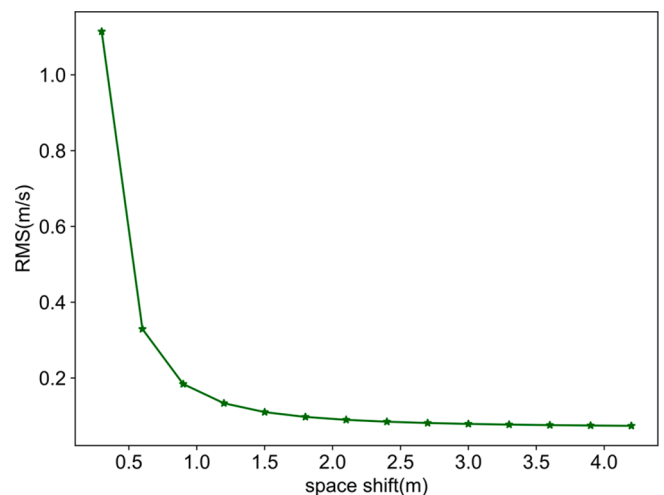

Fig. 11. Errors of the Mag-ODO versus the distance between the two magnetometers.

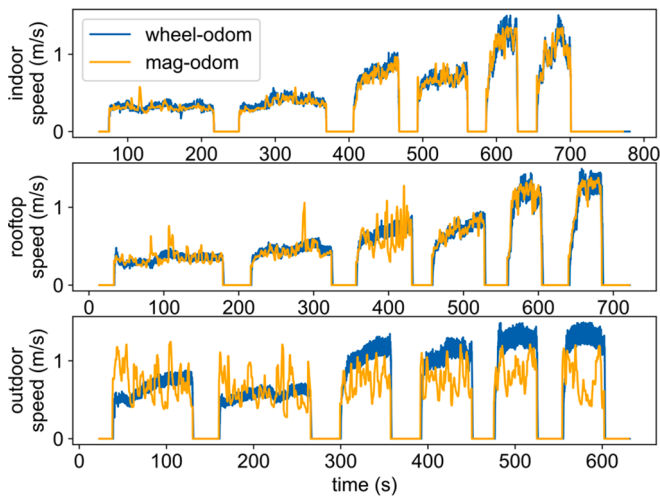**Fig. 12.** Errors of the Mag-ODO versus the travel distance in the matching windows.

Fig. 13. Speed curves comparison between Mag-ODO and wheel odometer in three different scenarios: indoor corridor, rooftop, and outdoor.

with rich magnetic field features, such as indoor or dense urban areas.

4.3. Dead reckoning performance Test

Although the previous tests were performed in a straight-line environment, it is important to evaluate the performance of the Mag-ODO in turn-case scenarios as well. To do this, we conducted two more complicated indoor tests, as shown in Fig. 14. Test 1 was set in an indoor circular corridor, where the robot moved for three laps. Test 2 was set in an indoor 8-shaped corridor, where the robot also moved for three laps. The experimental process is as follows. First, we obtained the speed from the magnetometer data. Next, we fused the speed and inertial information using the method described in Section 3. The initial position was set to the origin of the local navigation coordination system, and the initial heading was aligned with the local navigation coordination system.

The speed estimate curves and positioning results for Test 1 and Test 2 are shown in Fig. 15 and Fig. 16, respectively. The RMSEs of speed measurement for Test 1 and Test 2 are 0.052 m/s and 0.056 m/s, respectively. While calculating the positioning error of the entire trajectory can demonstrate the performance of the DR system, it is not optimal in the presence of trajectory loops. As shown in Fig. 15(c), the position error drifts in the opposite direction when the robot turns around. Therefore, we adopted the method proposed in [31] to evaluate
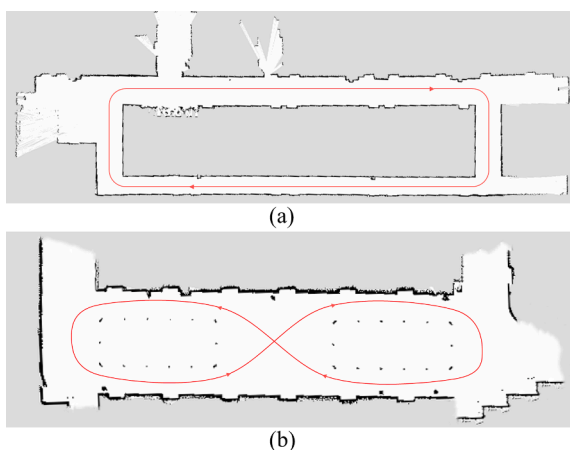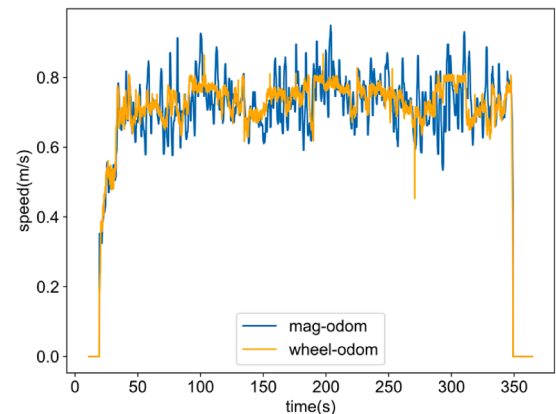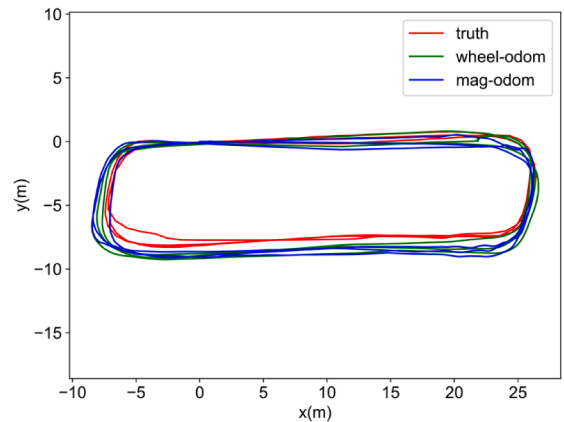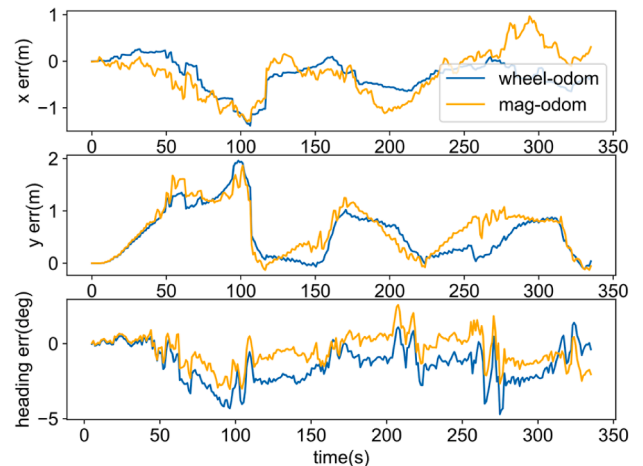

**Fig. 14.** Experimental environment and trajectories for the DR performance test: (a) Test 1; (b) Test 2.

Fig. 15. The result of Test 1: (a) Speed curves; (b) Estimated trajectories; (c) Positioning and heading errors.

the system's performance. First, we segmented the trajectory by a certain moving distance increment (l), then aligned the position and heading at the beginning of each segment and calculated the drift at the end. Finally, we computed the mean value (MEAN) and standard deviation (STD) of these segmented drift rates to evaluate the positioning performance. For this evaluation, we chose l to be 40 m. We calculated the maximum (MAX) and RMSE to evaluate the heading error. The error statistics of the Mag-ODO/INS and Wheel-ODO/INS are summarized in Table 3.

In both tests, the horizontal position drift rates of the Mag-ODO/INS

(a)

(b)

(c)
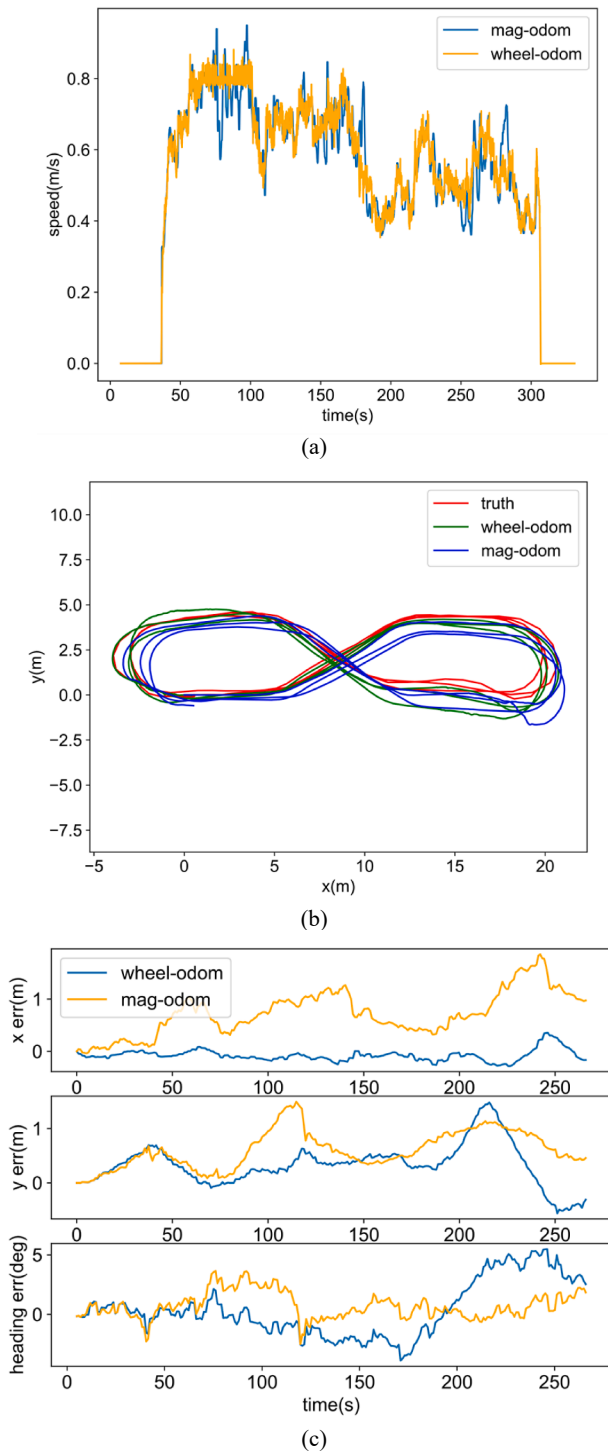
Fig. 16. The result of Test 2: (a) Speed curves; (b) Estimated trajectories; (c) Positioning and heading errors.

Table 3
the error statistics of Mag-ODO/INS and Wheel-ODO/INS.

Test	System	Position drift rate (%)		Heading error (°)	
		MEAN	STD	RMSE	MAX
1	Mag-ODO/INS	3.423	1.651	1.490	5.543
	Wheel-ODO/INS	3.754	1.678	2.450	6.986
2	Mag-ODO/INS	2.407	1.040	1.336	3.659
	Wheel-ODO/INS	2.412	2.388	2.362	5.487

were lower than 3.5 %, which is the same as the Wheel-ODO/INS. The average heading accuracy of the Mag-ODO/INS was improved by 41 % compared to the Wheel-ODO/INS. Furthermore, the DR performance of Test 2 was better than that of Test 1 due to the increased magnetic features caused by the iron railings (*i.e.*, the dots surrounded by the track in Test 2). Despite a deviation of approximately 0.06 m/s in RMSE between the speed measurements of the Mag-ODO and Wheel-ODO, the DR system based on the Mag-ODO achieved the same positioning performance as the Wheel-ODO and better heading accuracy.

It should be noted that if the magnetic field in the environment is fixed and there is no large fluctuating magnetic field, Mag-ODO is also applicable to this type of scenario. The test conclusions are also applicable to this type of scenario.

5. Conclusion and future works

In this study, we propose a motion speed estimation method for indoor robots based on dual magnetometers, named Mag-ODO, to enhance the robustness of the positioning system. High-precision speed estimates have been achieved using only two magnetometers with simple installation. Besides, the impact of temporary magnetic field gradient reductions within the time window has been properly addressed, exhibiting improved accuracy.

The experimental results demonstrate that Mag-ODO yields comparable performance to the traditional wheel odometer in environments with rich magnetic field features. We also investigate the factors that affect the speed estimation accuracy, including the distance between front and back magnetometers, travel distance in a fixed time window, and the complexity of magnetic field features. Furthermore, we test the DR system based on Mag-ODO/INS and find that it performs similar accuracy to the traditional Wheel-ODO/INS system in both straight and curved environments.

The proposed method has the potential to enhance the robustness and accuracy for indoor robots in complex environments. Nevertheless, the current implementation is only for one-dimensional speed estimation. More magnetometers can be employed for 3-DOF velocity perception. Besides, some means can be used to improve the performance of the proposed method, such as using deep learning methods to implement waveform matching, fusing the proposed method with SLAM to improve the positioning accuracy in degradation scenes, and adding an adaptive adjustment scheme for the time window length to balance the accuracy and efficiency.

CRediT authorship contribution statement

Tisheng Zhang: Conceptualization, Writing – review & editing, Funding acquisition. **Linfu Wei:** Methodology, Software, Data curation, Validation, Writing – original draft. **Jian Kuang:** Methodology, Writing – review & editing, Supervision. **Hailiang Tang:** Software, Data curation, Writing – review & editing. **Xiaoji Niu:** Conceptualization, Writing – review & editing, Supervision.

Declaration of Competing Interest

The authors declare that they have no known competing financial interests or personal relationships that could have appeared to influence the work reported in this paper.

Data availability

Data will be made available on request.

Acknowledgements

References

[1] S. Kuutti, S. Fallah, K. Katsaros, M. Dianati, F. Mccullough, A. Mouzakitis, A Survey of the state-of-the-art localization techniques and their potentials for autonomous vehicle applications, IEEE Internet Things J. 5 (2018) 829–846, https://doi.org/10.1109/JIOT.2018.2812300.

[2] D. Doberstein, Introduction to the Global Positioning System, in: D. Doberstein (Ed.), Fundamentals of GPS Receivers: A Hardware Approach, Springer, New York, NY, 2012, pp. 23–37.

[3] B.-S. Cho, W. Moon, W.-J. Seo, K.-R. Baek, A dead reckoning localization system for mobile robots using inertial sensors and wheel revolution encoding, J. Mech. Sci. Technol. 25 (2011) 2907–2917, https://doi.org/10.1007/s12206-011-0805-1.

[4] S.A.S. Mohamed, M.-H. Haghbayan, T. Westerlund, J. Heikkonen, H. Tenhunen, J. Plosila, A survey on odometry for autonomous navigation systems, IEEE Access 7 (2019) 97466–97486, https://doi.org/10.1109/ACCESS.2019.2929133.

[5] S. Du, W. Sun, Y. Gao, MEMS IMU Error mitigation using rotation modulation technique, Sensors 16 (2016) 2017, https://doi.org/10.3390/s16122017.

[6] J. Zhang, M. Kaess, S. Singh, On degeneracy of optimization-based state estimation problems, IEEE International Conference on Robotics and Automation (ICRA) 2016 (2016) 809–816, https://doi.org/10.1109/ICRA.2016.7487211.

[7] M.O.A. Aqel, M.H. Marhaban, M.I. Saripan, N.Bt. Ismail, Review of visual odometry: types, approaches, challenges, and applications, Springerplus 5 (2016) 1897, https://doi.org/10.1186/s40064-016-3573-7.

[8] H. Tang, X. Niu, T. Zhang, Y. Li, J. Liu, OdoNet: Untethered speed aiding for vehicle navigation without hardware wheeled odometer, IEEE Sens. J. 22 (2022) 12197–12208, https://doi.org/10.1109/JSEN.2022.3169549.

[9] L. Wang, X. Niu, T. Zhang, H. Tang, Q. Chen, Accuracy and robustness of ODO/NHC measurement models for wheeled robot positioning, Measurement 201 (2022), 111720, https://doi.org/10.1016/j.measurement.2022.111720.

[10] N. El-Sheimy, A. Youssef, Inertial sensors technologies for navigation applications: state of the art and future trends, Satellite Navigation. 1 (2020) 2, https://doi.org/10.1186/s43020-019-0001-5.

[11] L. Huang, Review on LiDAR-based SLAM Techniques, In: 2021 International Conference on Signal Processing and Machine Learning (CONF-SPML), 2021: pp. 163–168. https://doi.org/10.1109/CONF-SPML54095.2021.00040.

[12] D. Vissiere, A. Martin, N. Petit, Using magnetic disturbances to improve IMU-based position estimation, Proceedings of the European Control ConferencE 2007 (2007).

[13] D. Vissiere, A. Martin, N. Petit, Using distributed magnetometers to increase IMU-based velocity estimation into perturbed area, 2008. https://doi.org/10.1109/CDC.2007.4434809.

[14] P. Batista, N. Petit, C. Silvestre, P. Oliveira, Further results on the observability in magneto-inertial navigation, 2013. https://doi.org/10.1109/ACC.2013.6580210.

[15] C.-I. Chesneau, M. Hillion, C. Prieur, Motion estimation of a rigid body with an EKF using magneto-inertial measurements, in: 7th Conf. on Indoor Positioning and Indoor Navigation (IPIN'16), Madrid, Spain, 2016: pp. 1–6. https://doi.org/10.1109/IPIN.2016.7743702.

[16] M. Zmitri, H. Fourati, C. Prieur, Improving Inertial Velocity Estimation Through Magnetic Field Gradient-based Extended Kalman Filter, in: IPIN 2019 -

[17] I. Skog, G. Hendeby, F. Gustafsson, Magnetic Odometry - A Model-Based Approach Using a Sensor Array, in: 2018 21st International Conference on Information Fusion (FUSION), IEEE, Cambridge, United Kingdom, 2018: pp. 794–798. https://doi.org/10.23919/ICIF.2018.8455430.

[18] C.-I. Chesneau, Magneto-Inertial Dead-Reckoning in inhomogeneous field and indoor applications, phdthesis, Université Grenoble Alpes, 2018. https://theses.hal.science/tel-01966619.

[19] M. Zmitri, H. Fourati, C. Prieur, Magnetic field gradient-based EKF for velocity estimation in indoor navigation, Sensors 20 (2020) 5726, https://doi.org/10.3390/s20205726.

[20] I. Skog, G. Hendeby, F. Trulsson, Magnetic-field Based Odometry – An Optical Flow Inspired Approach, in: 2021 International Conference on Indoor Positioning and Indoor Navigation (IPIN), IEEE, Lloret de Mar, Spain, 2021: pp. 1–8. https://doi.org/10.1109/IPIN51156.2021.9662626.

[21] B. Kim, S.-H. Kong, A novel indoor positioning technique using magnetic fingerprint difference, IEEE Trans. Instrum. Meas. 65 (2016) 2035–2045, https://doi.org/10.1109/TIM.2016.2566759.

[22] W. Storms, J. Shockley, J. Raquet, Magnetic field navigation in an indoor environment, Ubiquitous Positioning Indoor Navigation and Location Based Service 2010 (2010) 1–10, https://doi.org/10.1109/UPINLBS.2010.5653681.

[23] K.P. Subbu, B. Gozick, R. Dantu, LocateMe: Magnetic-fields-based Indoor localization using smartphones, ACM Transactions on Intelligent Systems and Technology (TIST) 4 (4) (2013) 1–27.

[24] A.G. Asuero, A. Sayago, A.G. González, The correlation coefficient: An overview, Crit. Rev. Anal. Chem. 36 (2006) 41–59, https://doi.org/10.1080/10408340500526766.

[25] M. Müller, ed., Dynamic Time Warping, in: Information Retrieval for Music and Motion, Springer, Berlin, Heidelberg, 2007: pp. 69–84. https://doi.org/10.1007/978-3-540-74048-3_4.

[26] H. Wang, Y. Yu, Q. Yuan, Application of Dijkstra algorithm in robot path-planning, in, Second International Conference on Mechanic Automation and Control Engineering 2011 (2011) 1067–1069, https://doi.org/10.1109/MACE.2011.5987118.

[27] E.J. Keogh, M.J. Pazzani, Derivative Dynamic Time Warping, in: Proceedings of the 2001 SIAM International Conference on Data Mining (SDM), Society for Industrial and Applied Mathematics. 2001 pp. 1–11. https://doi.org/10.1137/1.9781611972719.1.

[28] E.-H. Shin, Estimation techniques for low-cost inertial navigation, UCGE Report. 20219 (2005).

[29] T. Liu, J. Kuang, W. Ge, P. Zhang, X. Niu, A simple positioning system for large-scale indoor patrol inspection using foot-mounted INS, QR Code Control Points, and Smartphone, IEEE Sensors Journal. 21 (2021) 4938–4948, https://doi.org/10.1109/JSEN.2020.3030934.

[30] W. Hess, D. Kohler, H. Rapp, D. Andor, Real-time loop closure in 2D LIDAR SLAM, IEEE International Conference on Robotics and Automation (ICRA) 2016 (2016) 1271–1278, https://doi.org/10.1109/ICRA.2016.7487258.

[31] Z. Zhang, D. Scaramuzza, A Tutorial on Quantitative Trajectory Evaluation for Visual(-Inertial) Odometry, In: 2018 IEEE/RSJ International Conference on Intelligent Robots and Systems (IROS), IEEE, Madrid, 2018: pp. 7244–7251. https://doi.org/10.1109/IROS.2018.8593941.